

Understanding the degradation of a model Si-anode in Li-ion battery at the atomic-scale

Se-Ho Kim^{1,†,*}, Kang Dong^{2,†}, Huan Zhao¹, Ayman A. El-Zoka¹, Xuyang Zhou¹, Eric V. Woods¹, Finn Giuliani³, Ingo Manke², Dierk Raabe¹, Baptiste Gault^{1,3,*}

¹ Max-Planck Institut für Eisenforschung GmbH, Max-Planck-Straße 1, 40237 Düsseldorf, Germany

² Institute of Applied Materials, Helmholtz-Zentrum Berlin für Materialien und Energie, Berlin, 14109 Germany

³ Department of Materials, Royal School of Mines, Imperial College, London, SW7 2AZ, United Kingdom

[†]these authors contributed equally

*Corr. Authors: s.kim@mpie.de, b.gault@mpie.de

Abstract

Si-anodes have long been candidates thanks to an expected ten-fold increase in capacity compared to graphite. However, details of the mechanisms governing their degradation remain elusive, hindering science-guided development of long-lived Si-based anodes. Here, to advance the understanding of the degradation of the electrolyte and electrode, and their interface, we exploit the latest developments in cryo-atom probe tomography to study a model, single crystal Si anode during cycling. We evidence anode corrosion from the decomposition of the Li-salt before charge-discharge cycles even begin. The newly created grain boundaries facilitate pulverization of nanoscale Si fragments, one is found floating in the electrolyte. As structural defects are bound to assist the nucleation of Li-rich phases in subsequent lithiations and accelerate the electrolyte's decomposition, these insights into the developed nanoscale microstructure interacting with the electrolyte contribute to understanding the self-catalysed/accelerated degradation Si-anodes and can inform new battery designs unaffected by these life-limiting factors.

Keywords: atom probe tomography • silicon anode • lithium ion battery • degradation

To meet the rapidly increasing demand for Li-ion batteries for electric vehicles^{1,2}, tremendous efforts have been devoted to discover cheap and abundant anode material that can replace graphite that is in short supply³. A crystalline Si anode, which can offer nearly ten times the capacity of a commercial graphite anode ($Q_{\text{Si}} = 3600 \text{ mAh g}^{-1}$ vs. $Q_{\text{graphite}} = 372 \text{ mAh g}^{-1}$)⁴, has emerged as an attractive anode material for next-generation Li-ion batteries since the first development of the Li-Si anode by Lai in 1976⁵. Compared to graphite, in which each of the six in-plane C atoms can only bond with one Li ion, each Si atom can bond with up to 4.4 Li ions⁶. Thus, finding a path to exploiting Si as anode material can be a revolutionary approach for reaching batteries with ultra-high energy density. Telsa Inc. has revealed its plans to gradually increase the use of Si anode in its future batteries⁷, and Amprius Tech. Inc. recently announced the shipment of its first commercially available Li-Si battery cells with energy density of 450 mWh g^{-1} ⁸.

An efficient Si anode remains some sort of *holy grail* for rechargeable Li-ion batteries, and their widespread use is hindered by rapid capacity fading^{9,10}. The enormous volume changes occurring during lithiation/delithiation cycles (*e.g.* +300 % volume increase from Si to $\text{Li}_{22}\text{Si}_5$) result in irreversible damage⁴: deformation and residual stresses accumulate and create an ensemble of structural defect features and their respective chemical decoration states, including interfaces, dislocations, grain boundaries, and nano-cracks forming within the Si anode. An array of approaches has been explored to overcome this critical issue. For example, the use of nano-composite/structured Si¹¹, including nanowires^{12,13}, core-shell^{14,15} and hollow^{16,17} nanoparticles, and porous Si^{18,19}, has been reported to be effective for the enhanced suppression of the initiation of mechanical fracture from the large volume changes.

Most studies use techniques providing a bulk average or two-dimensional information²⁰⁻²², which, even in combination, cannot analyse the nanoscale compositional distribution and microstructural evolution of electrodes and electrolytes. In-situ^{11,23,24} and cryogenic transmission electron microscopy (TEM)^{25,26} have already revealed an undesirable removal or destruction of the passivating solid-electrolyte interphase (SEI), and severe pulverization of Si nano/micro-particles from bulk Si during the expansion and shrinkage cycles²⁶. Despite impressive empirical advances, numerous fundamental aspects of the microstructural

degradation hence remain elusive, making it impossible to devise targeted strategies to circumvent these specific issues and enable a breakthrough in Si-based anodes. Elucidating the deformation that led to mechanical failure has emerged as a crucial topic to achieve a high-capacity Si anode.

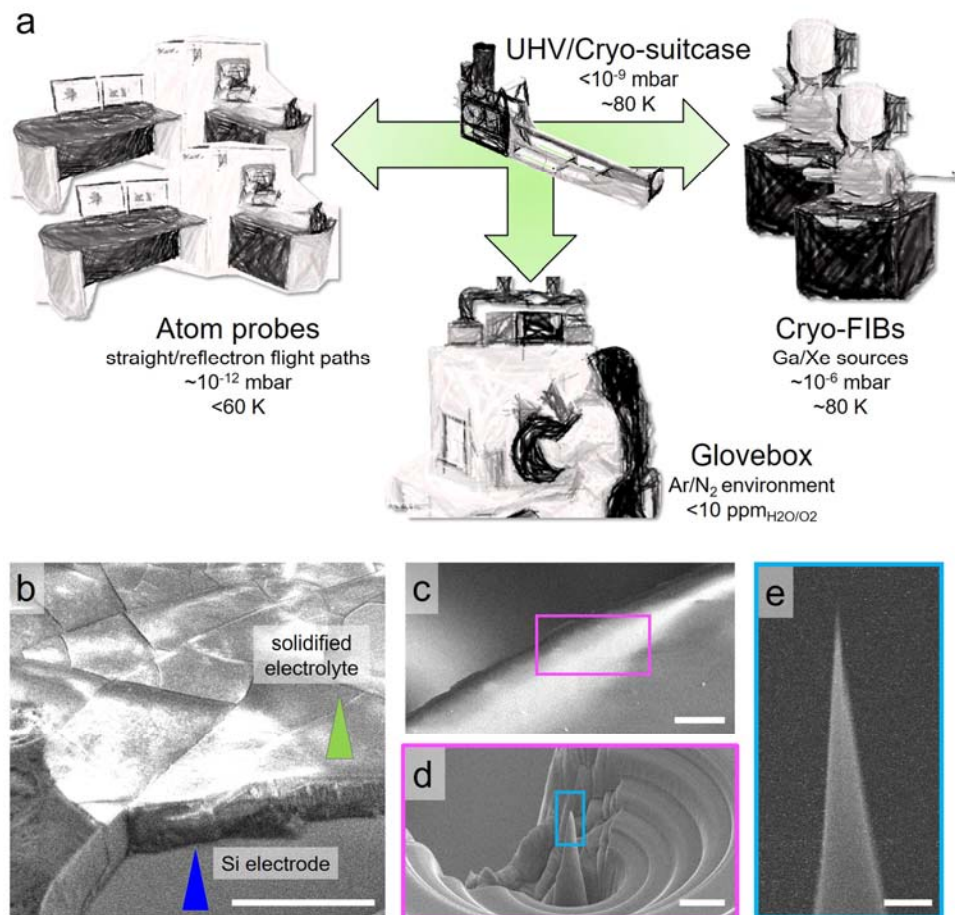


Figure 1. a) Unique infrastructure for cryo-atom probe enabling the study. (b) SEM images of the LN₂-quenched anode containing the frozen-electrolyte surface; (c) the Si electrode where the (d) cryo-milled pillar was made to prepare the (e) final APT specimen. Scale bars are 50 μ m in (b)&(c), 20 μ m in (d) and 1 μ m in (e).

The combination of high-resolution microscopy of the fine scale of the microstructure that develops, and the precise microanalysis of the electrode's evolving composition, can be achieved by using the latest development in cryogenic atom probe tomography (cryo-APT), Figure 1a. APT provides direct and three-dimensional, near-atomically resolved analytical imaging of materials and has the ability to collect all element irrespective of their mass. APT is underpinned by an intense electric field that provides controlled

removal of individual ions from a sharp, needle-shaped specimen. However, this field can cause outwards electromigration of Li²⁷ in battery materials, making impossible the detailed analysis of its distribution but also affecting the overall data quality²⁸, which explains why battery materials have rarely been analysed by APT^{29–32}. However, we demonstrated recently approaches enabling analysis of lithiated anode and cathode materials²⁸, and delithiated samples still bear traces of crucial processes taking place during battery operation.

Here, we leverage cryo-APT for the first time to obtain compositional mapping of Li-ion battery materials, the abutting electrolyte and the solid-liquid interface between the two at increasing number of charge-discharge cycles. Custom cells were disassembled inside a N₂ glovebox (H₂O and O₂ < 10ppm)³³, see Methods. The collected Si anode with the electrolyte were immediately plunge-frozen in liquid-N₂ (LN₂), then transferred by using the cryogenically-cooled, ultra-high-vacuum suitcases into a scanning-electron microscope / Xe-plasma focused ion beam (SEM/PFIB) for imaging and cryogenic specimen preparation, Figure 1b–c. APT specimens of the electrolyte and electrode were prepared at cryogenic temperature using the method we introduced in Ref.³⁴, Figure 1d–e.

The location of the cryo-APT analyses of the uncycled electrode and electrolyte, Figure 2c, are indicatively marked in Figure 1b. Within the electrolyte, individual, isolated Si ions are already detected. We conducted a cryo-APT analysis of the frozen raw electrolyte on a different metallic substrate (Au) that shows no Si ion (see Figure S1-S4). These additional analyses confirm that dissolved Si ions originated from the corrosion of the Si anode. Veith *et al.* observed non-electrochemically driven Si-O and Si-F bonds on a Si anode soaked in a similar electrolyte³⁵. Si-O groups can react with HF generated by hydrolyzed or thermally-decomposed LiPF₆ electrolyte³⁶, resulting in the dissolution of Si ions and two additional H₂O molecules, which trigger further HF generation and a self-sustaining corrosive cycle^{37–39}. The hydrolysis could be initiated by residual atmospheric moisture during cell assembly⁴⁰. Degradation of the anode and the electrolyte hence start even before cycling, with any oxygen-containing Si species that generate more water and accelerate the failure of the Si battery cell.

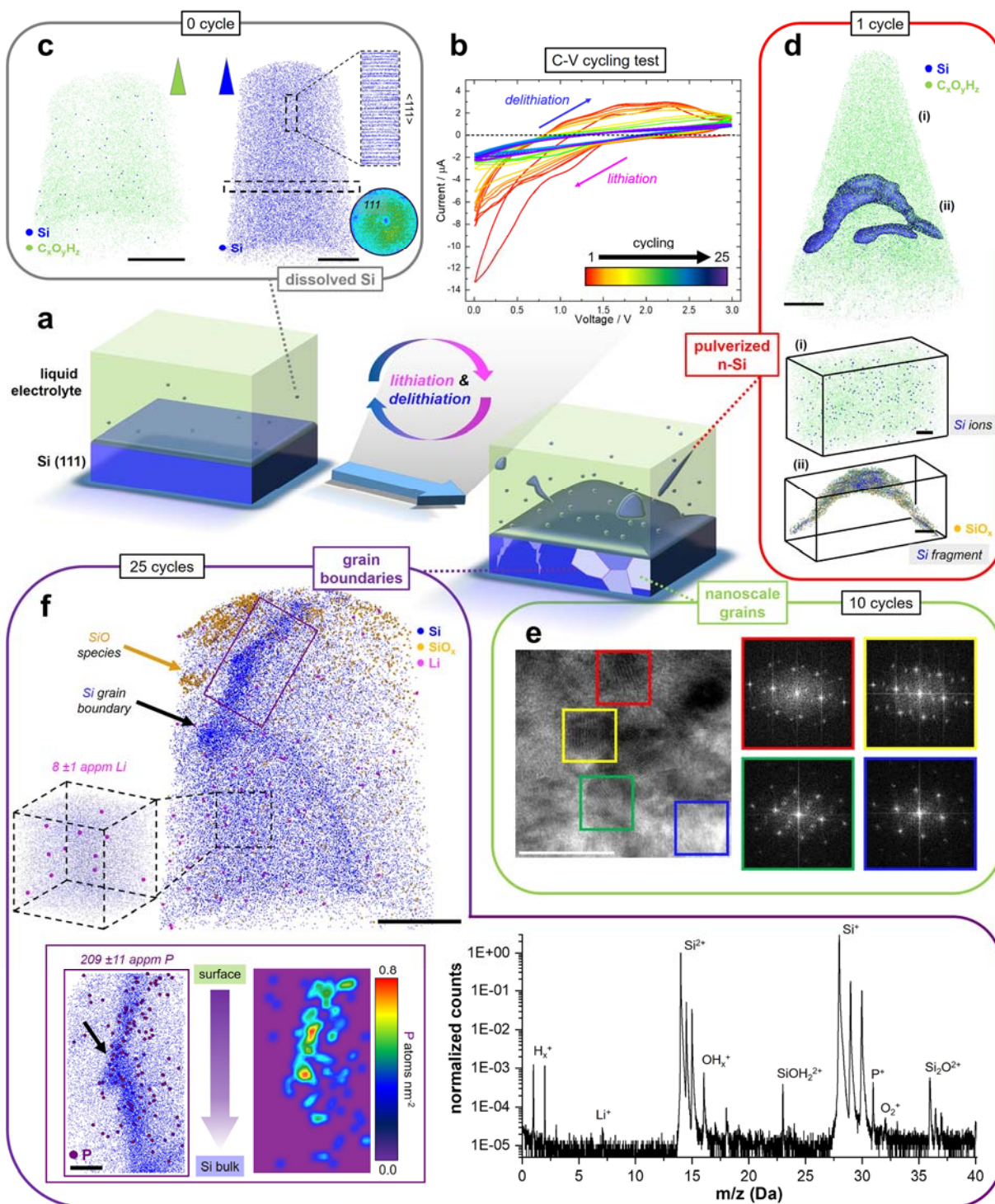


Figure 2. (a) Schematic of the Si electrode and cycling process. (b) Voltage vs. current curves of the Si(111) anode in a Li-Si cell. (c) cryo-APT analysis of the electrolyte and anode before cycling; scale bars are 20 nm. (d) cryo-APT reconstructed atom map of the 1-cycle electrolyte; the blue iso-surface delineates regions containing at least 25 at.% Si; scale bar is 20 nm. Movie (#1), the corresponding mass spectra and additional analyses can be found in SI; (i) is a close-up showing dissolved Si ions (scale bar = 2 nm) and (ii) is a delaminated Si debris in the electrolyte (scale bar = 5 nm). Green, blue, and yellow dots represent reconstructed carbonate species, Si and SiO_x compounds, respectively. (e) transmission-electron

micrograph of the 10-cycled Si anode along the [110] zone axis of the single-crystal, along with Fast Fourier Transformation (FFT) patterns from different regions highlighted by coloured boxes. A white scale bar is 20 nm. (f) 3D reconstructed atom map of the Si electrode after 25-cycles (scale bar = 20 nm). Blue, yellow, and pink dots represent reconstructed Si, SiO_x, and Li, respectively. Movie (#2) and mass spectra of corresponding dataset are presented in the SI. Inset shows the extracted Si grain boundary with the 2D contour density map of P atoms (scale bar = 5 nm).

After 1 cycle, Figure 1d, cryo-APT reveals also dissolved isolated Si ions, accompanied by an approx.10-nm pulverized Si fragment covered with an oxide shell (see Figure S5 and S6). Such a fragment could potentially block the pores of the separator for Li-ion diffusion, raising cell impedance and deteriorating the rate performance of the battery. The presence of the SiO_x-species at the surface support the hypothesis that the dissolution was associated to the formation of HF.

Already after 10-cycles, TEM was performed on the dried electrode after removal of the electrolyte and thorough cleaning, Figure 2e, complemented by additional APT experiments (Figure S7-S13). We evidences that the originally single crystalline Si has transformed into a nano-crystalline microstructure, containing numerous nanoscale grains and grain boundaries with different crystallographic orientations that have been formed during the lithiation/delithiation process, confirming previous reports⁴¹. The volume change associated with the formation of Li-rich phases imposes strong compressive loading on the silicon matrix⁴². Indentation of Si single-crystals has demonstrated that the breaking of covalent Si-Si bonds injects a high number of vacancies in the crystal and results in amorphization^{43,44}, also recently reported experimentally during battery cycling⁴⁵. Upon relaxation during delithiation, depending on the rate, new crystals nucleate with no orientation relationship with the surrounding crystal matrix^{43,44}. The discharging rate must influence this process.

After 25 cycles, Figure 2f, cryo-APT analysis of the very surface of the anode contains two Si grains, as confirmed by atom probe crystallography⁴⁶ (Figure S14), and a faceted grain boundary. No chemicals expected from the SEI layer (LiCO₂, LiOH, LiF) are observed at the interface (see Movie #3), which can be attributed to the high reversibility of the SEI layer on Si anodes^{25,47,48}. On the surface we find several isolated nanoscale islands rich in SiO_x species. Such oxides promote the formation of HF which corrodes the Si, passivate the Si anode and act as a mechanical clamping layer that restricts swelling^{48,49}. SiO_x can

store Li ions ($Q_{\text{SiO}} = 1543 \text{ mAh g}^{-1}$)⁵⁰ with lower volume expansion (approx. 120%) when irreversibly lithiated⁵¹, that can cause stress build-up at the interface and facilitate crack initiation⁵², decohesion and pulverization, explaining the presence of SiO_x on the Si fragment's surface in Figure 2d.

After full delithiation, 20-30nm below the surface, Li ($8 \pm 1 \text{ appm}$) is still detected within the Si matrix, as readily visible from the corresponding mass spectrum, Figure 2f. Density-functional theory predicts an attraction between vacancies and Li in Si^{53} , which can combine with a strong Coulomb attraction between an electron-rich vacancy and the electropositive Li. The image Li atoms are hence likely trapped by remaining vacancies injected under plastic loading.

At the grain boundary, Li does not appear segregated, conversely to P, that is even seen partitions to specific facets and to the facet junction indicated by a black arrow (see Figure S15). This distribution was previously suggested to be associated to local strain⁵⁴. P can diffuse along grain boundaries in Si^{55} , and its segregation can be energetically favourable due to the passivation of dangling bonds⁵⁶, which modifies the conductivity⁵⁷. In addition, atomistic simulations have indicated that the combined effect of the presence of P and a stress concentrator (i.e. a grain boundary) decreases the fracture strength of Si-nanowires⁵⁸. Lastly, the presence of P ($209 \pm 11 \text{ appm}$), originally from the LiPF_6 salt, also suggests the liberation of F and the facile formation of HF that is a known embrittler of polycrystalline-Si through void formation along grain boundaries⁵⁹. These effects collectively make these newly created grain boundaries particularly brittle and critical to the lifetime of the Si-anode.

To summarize, cryo-APT allowed us to track the evolution of the three-dimensional, nanoscale elemental distributions of species in the electrolyte, a model Si anode and their interface over increasing charge-discharge cycles. We provide measured data that advance the understanding of the degradation mechanism – or actually degradation mechanisms – and emphasise the often-overlooked role of microstructural defects created and evolving throughout the battery operation lifetime. In addition, the nucleation of the Li_xSi_y (metastable) phases⁴² during the first cycle can be assumed to be homogeneous, occurring randomly across the surface of the anode. However, the combined presence of crystalline defects and remaining Li-impurities in the anode will undoubtedly assist heterogeneous nucleation of these phases during subsequent

lithiation, potentially enhanced by accelerated diffusion of Li through structural defects^{60,61}. Segregants can energetically destabilize grain boundaries, already weakened by HF⁵⁹, or form space charges, that can favour decohesion. Nucleation in the parts of the microstructure with a high density of defects localizes the volume expansion to mechanically weaker regions, thus facilitating the pulverization of fragments from the anode. This combination of (electro)chemical reactions, phase transformation, and mechanical failure, assisted by the localised decomposition of the electrolyte, accelerates the delamination/mass loss and localized lithiation causing fast loss of capacity⁵¹ (see Figure S16). Strategies for the development of robust and durable Si-based anodes for next-generation Li-ion batteries can draw from our findings on the degradation of Si electrode –the role of the newly formed grain boundaries that may be exploited through segregation, but also the details of the electrolyte degradation that can guide the selection of P-free and F-free salts and avoiding exposure to moisture during fabrication, which can be difficult to achieve in large-scale production.

Acknowledgements

BG is grateful for fruitful discussions and insights from Dr. Christoph Freysoldt. SHK, EW, AEZ, BG are grateful for financial support from the ERC-CoG-SHINE-771602 at some point in the past few years. SHK, AEZ, DR, BG acknowledge financial support from the DFG through the DIP Project number 450800666. XZ is grateful for financial support from the Alexander von Humboldt Foundation.

References

- (1) Larcher, D.; Tarascon, J.-M. Towards Greener and More Sustainable Batteries for Electrical Energy Storage. *Nat. Chem.* 2014 71 **2014**, 7 (1), 19–29. <https://doi.org/10.1038/nchem.2085>.
- (2) JB Goodenough, K.-S. P. The Li-Ion Rechargeable Battery: A Perspective. *J. Am. Chem. Soc.* **2013**, 135 (4), 1167–1176. <https://doi.org/10.1021/ja3091438>.
- (3) Yan, Z.; Tom, D.; Maguire, G.; da Costa, A. N. China EV, Battery Makers Grapple with Graphite Squeeze. *Reuters*. December 15, 2021.
- (4) McDowell, M. T.; Lee, S. W.; Nix, W. D.; Cui, Y. 25th Anniversary Article: Understanding the Lithiation of Silicon and Other Alloying Anodes for Lithium-Ion Batteries. *Adv. Mater.* **2013**, 25 (36), 4966–4985. <https://doi.org/https://doi.org/10.1002/adma.201301795>.
- (5) Lai, S. Solid Lithium-Silicon Electrode. *J. Electrochem. Soc.* **1976**, 123 (8), 1196–1197. <https://doi.org/10.1149/1.2133033>.
- (6) Okamoto, H. Li-Si (Lithium-Silicon). *J. Phase Equilibria Diffus.* **2009**, 30 (1), 118–119. <https://doi.org/10.1007/s11669-008-9431-8>.
- (7) Telsa. 2020 Annual Meeting of Stockholders and Battery Day https://www.tesla.com/en_ca/2020shareholdermeeting.
- (8) Amprius Technologies, I. AMPRIUS TECHNOLOGIES SHIPS FIRST COMMERCIALY AVAILABLE 450 Wh/kg, 1150 Wh/L BATTERIES <https://amprius.com/2022/02/amprius-technologies-ships-first-commercially-available-450-wh-k-1150-wh-l-batteries> (accessed Feb 14, 2022).
- (9) Li, H.; Yamaguchi, T.; Matsumoto, S.; Hoshikawa, H.; Kumagai, T.; Okamoto, N. L.; Ichitsubo, T. Circumventing Huge Volume Strain in Alloy Anodes of Lithium Batteries. *Nat. Commun.* **2020**, 11 (1), 1584. <https://doi.org/10.1038/s41467-020-15452-0>.
- (10) Obrovac, M. N.; Chevrier, V. L. Alloy Negative Electrodes for Li-Ion Batteries. *Chem. Rev.* **2014**, 114 (23), 11444–11502. <https://doi.org/10.1021/cr500207g>.
- (11) Liu, X. H.; Zhong, L.; Huang, S.; Mao, S. X.; Zhu, T.; Huang, J. Y. Size-Dependent Fracture of Silicon Nanoparticles During Lithiation. *ACS Nano* **2012**, 6 (2), 1522–1531.

- <https://doi.org/10.1021/nn204476h>.
- (12) Chan, C. K.; Patel, R. N.; O'Connell, M. J.; Korgel, B. A.; Cui, Y. Solution-Grown Silicon Nanowires for Lithium-Ion Battery Anodes. *ACS Nano* **2010**, *4* (3), 1443–1450.
<https://doi.org/10.1021/nn901409q>.
- (13) Chan, C. K.; Peng, H.; Liu, G.; McIlwrath, K.; Zhang, X. F.; Huggins, R. A.; Cui, Y. High-Performance Lithium Battery Anodes Using Silicon Nanowires. *Nat. Nanotechnol.* **2008**, *3* (1), 31–35. <https://doi.org/10.1038/nnano.2007.411>.
- (14) Nava, G.; Schwan, J.; Boebinger, M. G.; McDowell, M. T.; Mangolini, L. Silicon-Core–Carbon-Shell Nanoparticles for Lithium-Ion Batteries: Rational Comparison between Amorphous and Graphitic Carbon Coatings. *Nano Lett.* **2019**, *19* (10), 7236–7245.
<https://doi.org/10.1021/acs.nanolett.9b02835>.
- (15) Zhang, T.; Gao, J.; Zhang, H. P.; Yang, L. C.; Wu, Y. P.; Wu, H. Q. Preparation and Electrochemical Properties of Core-Shell Si/SiO Nanocomposite as Anode Material for Lithium Ion Batteries. *Electrochem. commun.* **2007**, *9* (5), 886–890.
<https://doi.org/https://doi.org/10.1016/j.elecom.2006.11.026>.
- (16) Yao, Y.; McDowell, M. T.; Ryu, I.; Wu, H.; Liu, N.; Hu, L.; Nix, W. D.; Cui, Y. Interconnected Silicon Hollow Nanospheres for Lithium-Ion Battery Anodes with Long Cycle Life. *Nano Lett.* **2011**, *11* (7), 2949–2954. <https://doi.org/10.1021/nl201470j>.
- (17) Chen, Y.; Hu, Y.; Shen, Z.; Chen, R.; He, X.; Zhang, X.; Li, Y.; Wu, K. Hollow Core–Shell Structured Silicon@carbon Nanoparticles Embed in Carbon Nanofibers as Binder-Free Anodes for Lithium-Ion Batteries. *J. Power Sources* **2017**, *342*, 467–475.
<https://doi.org/https://doi.org/10.1016/j.jpowsour.2016.12.089>.
- (18) Ge, M.; Rong, J.; Fang, X.; Zhou, C. Porous Doped Silicon Nanowires for Lithium Ion Battery Anode with Long Cycle Life. *Nano Lett.* **2012**, *12* (5), 2318–2323.
<https://doi.org/10.1021/nl300206e>.
- (19) Xiao, J.; Xu, W.; Wang, D.; Choi, D.; Wang, W.; Li, X.; Graff, G. L.; Liu, J.; Zhang, J.-G.

- Stabilization of Silicon Anode for Li-Ion Batteries. *J. Electrochem. Soc.* **2010**, *157* (10), A1047.
<https://doi.org/10.1149/1.3464767>.
- (20) Schellenberger, M.; Golnak, R.; Quevedo Garzon, W. G.; Risse, S.; Seidel, R. Accessing the Solid Electrolyte Interphase on Silicon Anodes for Lithium-Ion Batteries in-Situ through Transmission Soft X-Ray Absorption Spectroscopy. *Mater. Today Adv.* **2022**, *14*, 100215.
<https://doi.org/10.1016/J.MTADV.2022.100215>.
- (21) Wang, L.; Menakath, A.; Han, F.; Wang, Y.; Zavalij, P. Y.; Gaskell, K. J.; Borodin, O.; Iuga, D.; Brown, S. P.; Wang, C.; et al. Identifying the Components of the Solid–Electrolyte Interphase in Li-Ion Batteries. *Nat. Chem.* *2019 119* **2019**, *11* (9), 789–796. <https://doi.org/10.1038/s41557-019-0304-z>.
- (22) Chen, C.; Zhou, T.; Danilov, D. L.; Gao, L.; Benning, S.; Schön, N.; Tardif, S.; Simons, H.; Hausen, F.; Schüllli, T. U.; et al. Impact of Dual-Layer Solid-Electrolyte Interphase Inhomogeneities on Early-Stage Defect Formation in Si Electrodes. *Nat. Commun.* *2020 111* **2020**, *11* (1), 1–10. <https://doi.org/10.1038/s41467-020-17104-9>.
- (23) McDowell, M. T.; Lee, S. W.; Harris, J. T.; Korgel, B. A.; Wang, C.; Nix, W. D.; Cui, Y. In Situ TEM of Two-Phase Lithiation of Amorphous Silicon Nanospheres. *Nano Lett.* **2013**, *13* (2), 758–764. <https://doi.org/10.1021/nl3044508>.
- (24) McDowell, M. T.; Ryu, I.; Lee, S. W.; Wang, C.; Nix, W. D.; Cui, Y. Studying the Kinetics of Crystalline Silicon Nanoparticle Lithiation with In Situ Transmission Electron Microscopy. *Adv. Mater.* **2012**, *24* (45), 6034–6041. <https://doi.org/https://doi.org/10.1002/adma.201202744>.
- (25) Huang, W.; Wang, J.; Braun, M. R.; Zhang, Z.; Li, Y.; Boyle, D. T.; McIntyre, P. C.; Cui, Y. Dynamic Structure and Chemistry of the Silicon Solid-Electrolyte Interphase Visualized by Cryogenic Electron Microscopy. *Matter* **2019**, *1* (5), 1232–1245.
<https://doi.org/https://doi.org/10.1016/j.matt.2019.09.020>.
- (26) He, Y.; Jiang, L.; Chen, T.; Xu, Y.; Jia, H.; Yi, R.; Xue, D.; Song, M.; Genc, A.; Bouchet-Marquis, C.; et al. Progressive Growth of the Solid–Electrolyte Interphase towards the Si Anode

- Interior Causes Capacity Fading. *Nat. Nanotechnol.* **2021**, *16* (10), 1113–1120.
<https://doi.org/10.1038/s41565-021-00947-8>.
- (27) Pfeiffer, B.; Maier, J.; Arlt, J.; Nowak, C. In Situ Atom Probe Deintercalation of Lithium-Manganese-Oxide. *Microsc. Microanal.* **2017**, *23* (2), 314–320.
<https://doi.org/10.1017/S1431927616012691>.
- (28) Kim, S.; Antonov, S.; Zhou, X.; Stephenson, L.; Jung, C.; El-Zoka, A.; Schreiber, D. K.; Conroy, S.; Gault, B.; Mater, J.; et al. Atom Probe Analysis of Electrode Materials for Li-Ion Batteries: Challenges and Ways Forward. *J. Mater. Chem. A* **2022**, *6*, 4883–5230.
<https://doi.org/10.1039/D1TA10050E>.
- (29) Devaraj, A.; Gu, M.; Colby, R.; Yan, P.; Wang, C. M.; Zheng, J. M.; Xiao, J.; Genc, A.; Zhang, J. G.; Belharouak, I.; et al. Visualizing Nanoscale 3D Compositional Fluctuation of Lithium in Advanced Lithium-Ion Battery Cathodes. *Nat. Commun.* **2015**, *6*.
<https://doi.org/10.1038/ncomms9014>.
- (30) Mohanty, D.; Mazumder, B.; Devaraj, A.; Sefat, A. S.; Huq, A.; David, L. A.; Payzant, E. A.; Li, J.; Wood, D. L.; Daniel, C. Resolving the Degradation Pathways in High-Voltage Oxides for High-Energy-Density Lithium-Ion Batteries; Alternation in Chemistry, Composition and Crystal Structures. *Nano Energy* **2017**, *36*, 76–84. <https://doi.org/10.1016/j.nanoen.2017.04.008>.
- (31) Chae, B.-G.; Park, S. Y.; Song, J. H.; Lee, E.; Jeon, W. S. Evolution and Expansion of Li Concentration Gradient during Charge–Discharge Cycling. *Nat Commun.* **2021**, *12* (1), 3814.
<https://doi.org/10.1038/s41467-021-24120-w>.
- (32) Maier, J.; Pfeiffer, B.; Volkert, C. A.; Nowak, C. Three-Dimensional Microstructural Characterization of Lithium Manganese Oxide with Atom Probe Tomography. *Energy Technol.* **2016**, *4* (12), 1565–1574. <https://doi.org/10.1002/ENTE.201600210>.
- (33) Stephenson, L. T.; Szczepaniak, A.; Mouton, I.; Kristiane, A.; Rusitzka, K.; Breen, A. J.; Tezins, U.; Sturm, A.; Vogel, D.; Chang, Y.; et al. The Laplace Project : An Integrated Suite for Preparing and Transferring Atom Probe Samples under Cryogenic and UHV Conditions. **2018**, 1–13.

- (34) El-Zoka, A. A.; Kim, S.-H.; Deville, S.; Newman, R. C.; Stephenson, L. T.; Gault, B. Enabling Near-Atomic-Scale Analysis of Frozen Water. *Sci. Adv.* **2020**, *6* (49), eabd6324. <https://doi.org/10.1126/sciadv.abd6324>.
- (35) Veith, G. M.; Baggetto, L.; Sacci, R. L.; Unocic, R. R.; Tenhaeff, W. E.; Browning, J. F. Direct Measurement of the Chemical Reactivity of Silicon Electrodes with LiPF₆-Based Battery Electrolytes. *Chem. Commun.* **2014**, *50* (23), 3081–3084. <https://doi.org/10.1039/C3CC49269A>.
- (36) McBrayer, J. D.; Rodrigues, M.-T. F.; Schulze, M. C.; Abraham, D. P.; Apblett, C. A.; Bloom, I.; Carroll, G. M.; Colclasure, A. M.; Fang, C.; Harrison, K. L.; et al. Calendar Aging of Silicon-Containing Batteries. *Nat. Energy* **2021**, *6* (9), 866–872. <https://doi.org/10.1038/s41560-021-00883-w>.
- (37) Lehmann, V. The Chemical Dissolution of Silicon. *Electrochemistry of Silicon*. February 22, 2002, pp 23–38. <https://doi.org/https://doi.org/10.1002/3527600272.ch2>.
- (38) Saqib, N.; Ganim, C. M.; Shelton, A. E.; Porter, J. M. On the Decomposition of Carbonate-Based Lithium-Ion Battery Electrolytes Studied Using Operando Infrared Spectroscopy. *J. Electrochem. Soc.* **2018**, *165* (16), A4051–A4057. <https://doi.org/10.1149/2.1051816jes>.
- (39) Agubra, V. A.; Fergus, J. W. The Formation and Stability of the Solid Electrolyte Interface on the Graphite Anode. *J. Power Sources* **2014**, *268*, 153–162. <https://doi.org/https://doi.org/10.1016/j.jpowsour.2014.06.024>.
- (40) Wiemers-Meyer, S.; Jeremias, S.; Winter, M.; Nowak, S. Influence of Battery Cell Components and Water on the Thermal and Chemical Stability of LiPF₆ Based Lithium Ion Battery Electrolytes. *Electrochim. Acta* **2016**, *222*, 1267–1271. <https://doi.org/https://doi.org/10.1016/j.electacta.2016.11.100>.
- (41) Shi, F.; Song, Z.; Ross, P. N.; Somorjai, G. A.; Ritchie, R. O.; Komvopoulos, K. Failure Mechanisms of Single-Crystal Silicon Electrodes in Lithium-Ion Batteries. *Nat. Commun.* **2016**, *7* (1), 11886. <https://doi.org/10.1038/ncomms11886>.
- (42) Chan, M. K. Y.; Wolverton, C.; Greeley, J. P. First Principles Simulations of the Electrochemical

- Lithiation and Delithiation of Faceted Crystalline Silicon. *J. Am. Chem. Soc.* **2012**, *134* (35), 14362–14374. <https://doi.org/10.1021/ja301766z>.
- (43) Ruffell, S.; Bradby, J. E.; Williams, J. S. High Pressure Crystalline Phase Formation during Nanoindentation: Amorphous versus Crystalline Silicon. *Appl. Phys. Lett.* **2006**, *89* (9), 91919. <https://doi.org/10.1063/1.2339039>.
- (44) Vandeperre, L. J.; Giuliani, F.; Lloyd, S. J.; Clegg, W. J. The Hardness of Silicon and Germanium. *Acta Mater.* **2007**, *55* (18), 6307–6315. <https://doi.org/https://doi.org/10.1016/j.actamat.2007.07.036>.
- (45) Mozhzhukhina, N.; Flores, E.; Lundström, R.; Nyström, V.; Kitz, P. G.; Edström, K.; Berg, E. J. Direct Operando Observation of Double Layer Charging and Early Solid Electrolyte Interphase Formation in Li-Ion Battery Electrolytes. *J. Phys. Chem. Lett.* **2020**, *11* (10), 4119–4123. https://doi.org/10.1021/ACS.JPCLETT.0C01089/SUPPL_FILE/JZ0C01089_SI_001.PDF.
- (46) Gault, B.; Moody, M. P.; Cairney, J. M.; Ringer, S. P. Atom Probe Crystallography. *Materials Today*. 2012. [https://doi.org/10.1016/S1369-7021\(12\)70164-5](https://doi.org/10.1016/S1369-7021(12)70164-5).
- (47) Zhang, X.; Weng, S.; Yang, G.; Li, Y.; Li, H.; Su, D.; Gu, L.; Wang, Z.; Wang, X.; Chen, L. Interplay between Solid-Electrolyte Interphase and (in)Active Li_xSi in Silicon Anode. *Cell Reports Phys. Sci.* **2021**, *2* (12), 100668. <https://doi.org/https://doi.org/10.1016/j.xcrp.2021.100668>.
- (48) Wu, H.; Chan, G.; Choi, J. W.; Ryu, I.; Yao, Y.; McDowell, M. T.; Lee, S. W.; Jackson, A.; Yang, Y.; Hu, L.; et al. Stable Cycling of Double-Walled Silicon Nanotube Battery Anodes through Solid–Electrolyte Interphase Control. *Nat. Nanotechnol.* **2012**, *7* (5), 310–315. <https://doi.org/10.1038/nnano.2012.35>.
- (49) Sivonxay, E.; Aykol, M.; Persson, K. A. The Lithiation Process and Li Diffusion in Amorphous SiO_2 and Si from First-Principles. *Electrochim. Acta* **2020**, *331*, 135344. <https://doi.org/https://doi.org/10.1016/j.electacta.2019.135344>.
- (50) Zhao, J.; Lee, H.-W.; Sun, J.; Yan, K.; Liu, Y.; Liu, W.; Lu, Z.; Lin, D.; Zhou, G.; Cui, Y.

- Metallurgically Lithiated SiO₂ Anode with High Capacity and Ambient Air Compatibility. *Proc. Natl. Acad. Sci.* **2016**, *113* (27), 7408 LP – 7413.
<https://doi.org/10.1073/pnas.1603810113>.
- (51) Pan, K.; Zou, F.; Canova, M.; Zhu, Y.; Kim, J.-H. Systematic Electrochemical Characterizations of Si and SiO Anodes for High-Capacity Li-Ion Batteries. *J. Power Sources* **2019**, *413*, 20–28.
<https://doi.org/https://doi.org/10.1016/j.jpowsour.2018.12.010>.
- (52) Kontis, P.; Li, Z.; Segersäll, M.; Moverare, J. J. J. J.; Reed, R. C. C. R. C.; Raabe, D.; Gault, B. The Role of Oxidized Carbides on Thermal-Mechanical Performance of Polycrystalline Superalloys. *Metall. Mater. Trans. A* **2018**, *49* (9), Accepted. <https://doi.org/10.1007/s11661-018-4709-x>.
- (53) Huang, J.; Wang, Z.; Gong, X.; Wu, M.; Liu, G.; Lei, X.; Liang, J.; Cao, H.; Tang, F.; Lei, M.; et al. Vacancy Assisted Li Intercalation in Crystalline Si as Anode Materials for Lithium Ion Batteries. *Int. J. Electrochem. Sci* **2013**, *8*, 5643–5649.
- (54) Liebscher, C. H.; Stoffers, A.; Alam, M.; Lymperakis, L.; Cojocaru-Mirédin, O.; Gault, B.; Neugebauer, J.; Dehm, G.; Scheu, C.; Raabe, D. Strain-Induced Asymmetric Line Segregation at Faceted Si Grain Boundaries. *Phys. Rev. Lett.* **2018**, *121* (1), 15702.
<https://doi.org/10.1103/PhysRevLett.121.015702>.
- (55) Holloway, P. H. Grain Boundary Diffusion of Phosphorus in Polycrystalline Silicon. *J. Vac. Sci. Technol.* **1982**, *21* (1), 19–22. <https://doi.org/10.1116/1.571713>.
- (56) Zhao, D.; Li, Y. Revealing the Factors Influencing Grain Boundary Segregation of P, As in Si: Insights from First-Principles. *Acta Mater.* **2019**, *168*, 52–62.
<https://doi.org/10.1016/J.ACTAMAT.2019.02.014>.
- (57) Carabelas, A.; Nobili, D.; Solmi, S. GRAIN BOUNDARY SEGREGATION IN SILICON HEAVILY DOPED WITH PHOSPHORUS AND ARSENIC. *J. Phys. Colloq.* **1982**, *43* (C1), C1-187-C1-192.
- (58) Liu, B.; Tao, J. Y.; Chen, X.; Zhang, Y. A.; Jiang, Y.; Qian, Y. Numerical Investigation of the

- Effects of Phosphorus on the Mechanical Responses of [1 1 0]-Oriented Silicon Nano-Wires. *Microelectron. Reliab.* **2016**, *64*, 225–229. <https://doi.org/10.1016/J.MICROREL.2016.07.070>.
- (59) Kageyama, Y.; Murase, Y.; Tsuchiya, T.; Funabashi, H.; Sakata, J. Formation of Porous Grain Boundaries in Polycrystalline Silicon Thin Films. *J. Appl. Phys.* **2002**, *91* (11), 9408. <https://doi.org/10.1063/1.1476088>.
- (60) Peng, Z.; Meiners, T.; Lu, Y.; Liebscher, C. H.; Kostka, A.; Raabe, D.; Gault, B. Quantitative Analysis of Grain Boundary Diffusion, Segregation and Precipitation at a Sub-Nanometer Scale. *Acta Mater.* **2022**, *225*, 117522. <https://doi.org/10.1016/J.ACTAMAT.2021.117522>.
- (61) Legros, M.; Dehm, G.; Arzt, E.; Balk, T. J. J. Observation of Giant Diffusivity Along Dislocation Cores. *Science (80-.)*. **2008**, *319* (5870), 1646–1649. <https://doi.org/10.1126/science.1151771>.

Supplementary Information

Understanding the degradation of a model Si-anode in Li-ion battery at the atomic-scale

Authors: Se-Ho Kim^{1,†,*}, Kang Dong^{2,†}, Huan Zhao¹, Ayman A. El-Zoka¹, Xuyang Zhou¹, Eric V. Woods¹, Finn Giuliani³, Ingo Manke², Dierk Raabe¹, Baptiste Gault^{1,3,*}

Affiliations:

¹Max-Planck-Institut für Eisenforschung GmbH, Max-Planck-Straße 1, 40237 Düsseldorf, Germany

²Institute of Applied Materials, Helmholtz-Zentrum Berlin für Materialien and Energie, 14109 Berlin, Germany

³Department of Materials, Royal School of Mines, Imperial College, SW7 2AZ London, United Kingdom

†co-first authors

*corresponding authors

Methods

Materials

Silicon wafer (0.5 mm thick, no dopant, (111)) and an electrolyte of 1 M LiPF₆ with a mixture of ethylene carbonate (EC) and diethyl carbonate (DEC) (1:1, v/v) were received from Sigma-Aldrich. Metallic lithium was purchased from MTI Corp. USA. A Swagelok derived cell consisting of a polyether ether ketone (PEEK) housing is described in our previous report⁶⁷.

Battery Assembly and Cycling

Si wafer was cut into 3.0 mm disks by laser-cutting under Argon gas protection. The obtained Si disks were washed using ultrapure water (Milli-Q) and 2-propanol (HPLC Plus, 99.9%, Sigma-Aldrich) to remove contaminations (*e.g.* dust) on the surface from the cutting process. Li chips were punched into disks with a diameter of 3 mm as the counter electrode without further treatment. To preserve the SEI layer on the surface of Si wafer, instead of using a typical Celgard or glassfiber separator, we opt for a ring-shaped spacer (0.5 mm thick) made of polytetrafluoroethylene (PTFE) as a separator. In this way, the Si surface including the SEI layer at the middle area of the Si disk could keep intact without undergoing a peeling-off procedure during the cell disassembly. The Li/Si cells were built using the customized Swagelok-type cell in an argon-filled MBraun glovebox (H₂O and O₂ < 5 ppm). After cell assembly, Li/Si cells were subjected to cyclic voltammetry (CV) cycling between 0.01 – 3.0 V at a scan rate of 0.2 mV/s using a BioLogic MPG-200 potentiostat. All the cells were stopped after 0, 1, 10, 25 cycles at the delithiation state (see Fig. S17).

Sample preparation

After cycling, the cell was disassembled in a nitrogen filled glove-box (<10 ppm H₂O and O₂). Without washing, the Si disk was mounted on a Cu clip and was rapidly plunged into liquid nitrogen, followed by loading on a scanning-electron microscope/Xe-plasma focused ion beam (SEM/p-FIB) (Helios PFIB, Thermo-Fisher, Eindhoven, Netherlands) stage. Subsequently, the Si disk was transferred into the cryo-p-

FIB chamber using the ultra-high vacuum transfer suitcase (10^{-9} mbar, -190 °C) (VSN-40, Ferrovac GmbH, Zurich, Switzerland) to avoid the sample exposure to air. An illustration of environmentally sensitive sample preparation/transfer for FIB/APT is shown in Fig. S18.

Cryo-APT specimen preparation

The cryo-p-FIB stage (Gatan C1001, Gatan Inc., California, USA) was pre-cooled to -190 °C by cold N_2 gas. A clean pillar from frozen electrolyte and Si anode was prepared using the in-situ non lift-out protocol described in references^{32,68}. After the height of the post had reached 50 μm , progressively the frozen sample were sharpened into APT specimen using annular milling patterns (e.g. specimen-radius less than 100 nm). Scanning electron micrographs were taken at 5 - 15 kV and 1.6 - 2.3 nA to avoid charging effects and the e-beam-induced diffusion/reaction (see Fig. S19 and S20).

APT measurement

Atom probe data were acquired from 5000 XS instrument (CAMECA, Madison, USA) in pulsed laser mode with laser energy of 20 - 40 pJ for the cold Si anode (80 pJ for the frozen electrolytes) and rate of 100 kHz at 1 % detection rate. The base temperature was set to 60 K throughout the measurement and the applied direct current was adjusted to control the stable evaporation (see Fig. S21). The atom map reconstruction and data analysis were done using AP SUITE 6.1 software developed by CAMECA.

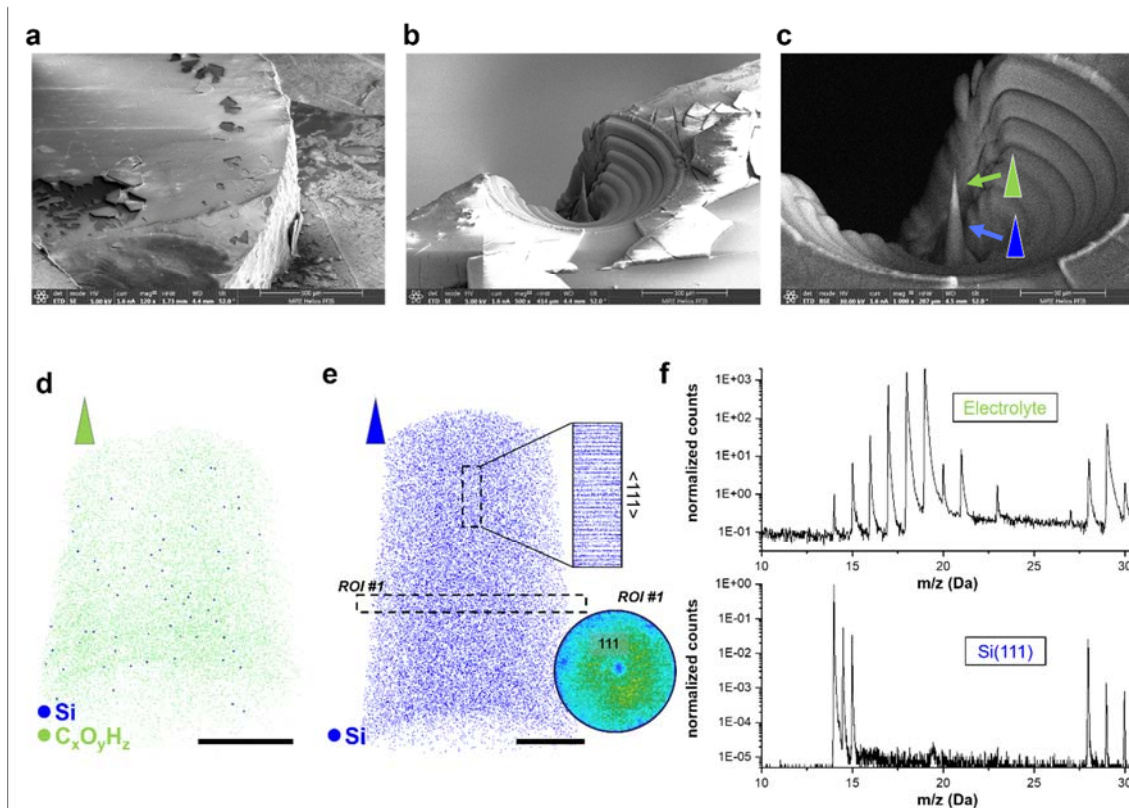


Fig. S1. (a) SEM image of frozen 0-cycle Si anode. (b) In-situ annular milling process. (c) Final APT specimens. 3D atom maps of the 0-cycle specimen: (d) electrolyte and (e) single crystal Si(111) anode. Scale bars are 20 nm. (f) corresponding mass spectrum of each. Here in the electrolyte mass-spectrum, no Li peaks were measured; however, we detected a strong peak at 19-21 Da which could be originated from LiC^+ (or F^+) and LiCH_x^+ (or $\text{H}_x\text{F}/\text{LiO}_x^+$) species. Nevertheless, herein, no segregation behavior of carbonate species nor no LiPF_6 salt are detected. The decomposed C:O atomic ratio from the acquired mass spectrum is 1.07 which supports that the frozen specimen is the electrolyte compound. The molecular formulae of mixed organic solvent of ethyl carbonate (EC) and dimethyl carbonate (DMC) compounds are $\text{C}_3\text{O}_3\text{H}_4$ and $\text{C}_3\text{O}_3\text{H}_6$, respectively, so it is difficult to conclude which molecules they are. Apart from that, as expected, the atom map of the as-received single-crystal Si anode shows [111] crystallographic pole at the center with Si(111) atomic planes readily visible.

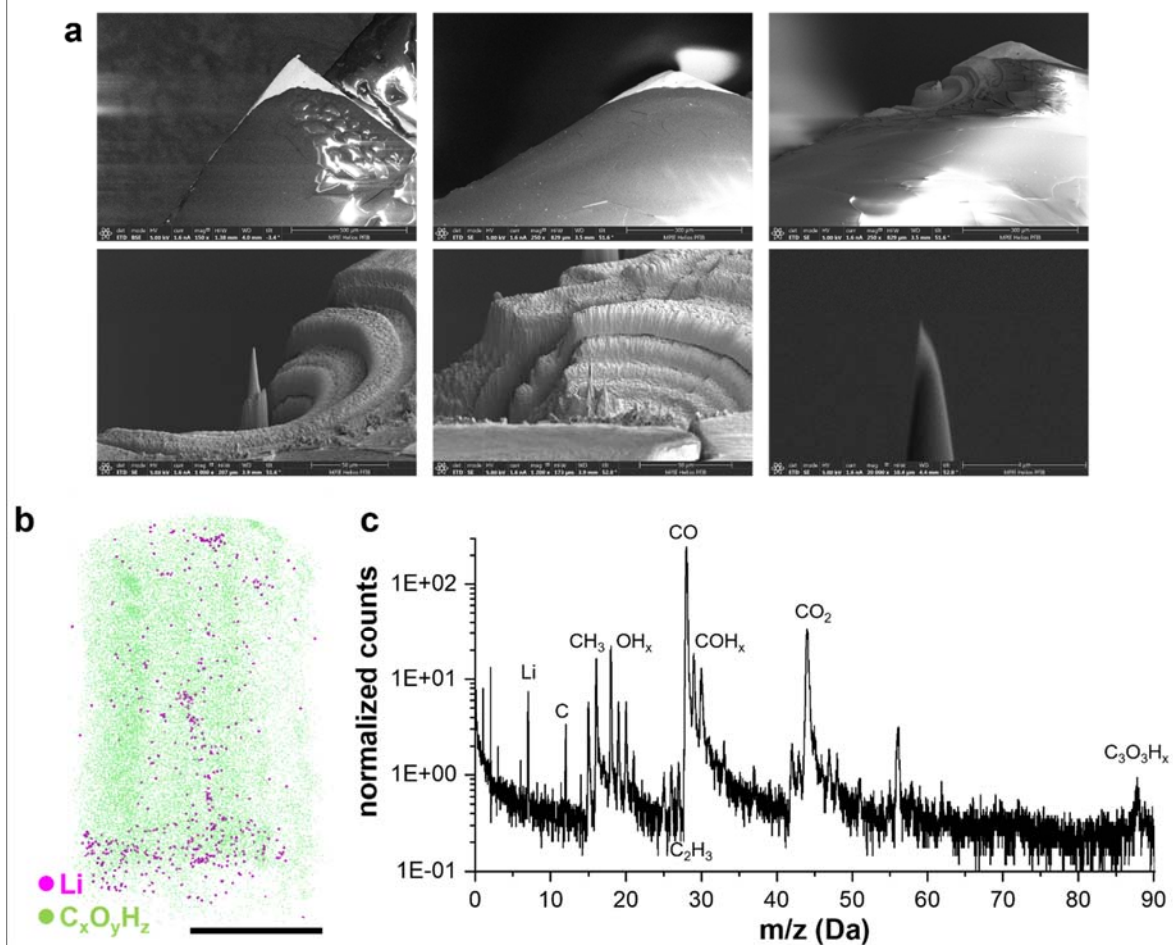


Fig. S2. (a) Cryo-APT specimen preparation from a raw electrolyte (non-contact with Si). (b) 3D atom map of a raw electrolyte (a scale bar = 20 nm) and (c) corresponding mass spectrum. Note that there are no Si peaks. Nano-porous gold instead of Si was used as a substrate to hold the frozen raw liquid electrolyte for cryo-APT measurement. The reconstructed Li ions (6,7 Da) are segregated locally implying that there was a phase separation of the Li salt during freezing. In the mass spectrum of the pristine (non-Si contacted) electrolyte, notable peaks at 90-85 Da are measured which originates to the $C_3O_3H_x^+$ molecular species.

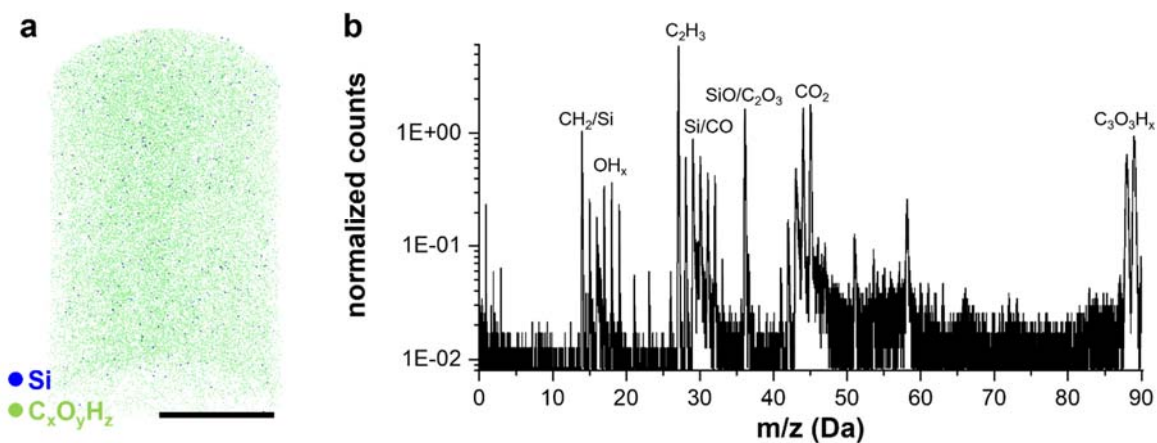


Fig. S3. Additional cryo-APT measurement of the 1-cycle electrolyte. (a) 3D atom map of 1-cycle electrolyte and (b) corresponding mass spectrum. Note that there is Si peaks. A scale bar is 20 nm.

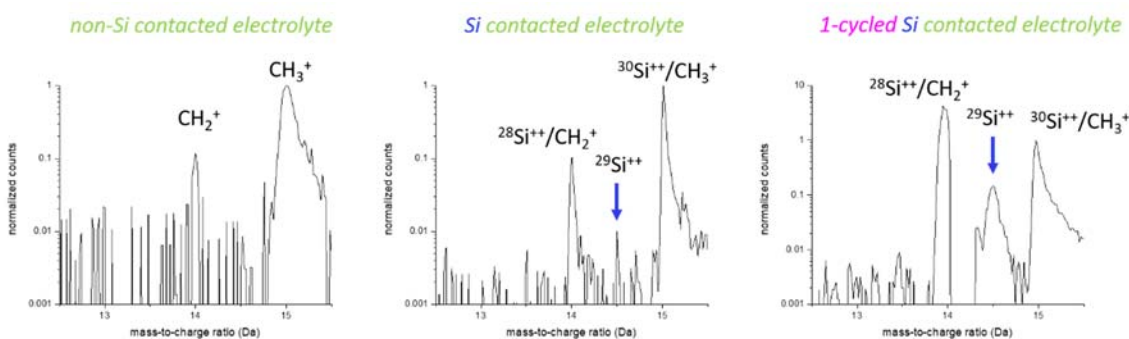


Fig. S4. Background corrected mass spectra of non-Si, Si-contacted and 1-cycled electrolyte. Note that peaks at 14.5 Da aren't likely from CO^{++} state. The second ionization energy of CO requires 41.8 ± 0.5 eV (for $\text{CO}^+ = 14.07 \pm 0.05$ eV)¹ whereas ionization energies of Si^+ and Si^{++} are 8.15 and 16.34 eV. Therefore, detecting CO^{++} is extremely unlikely.

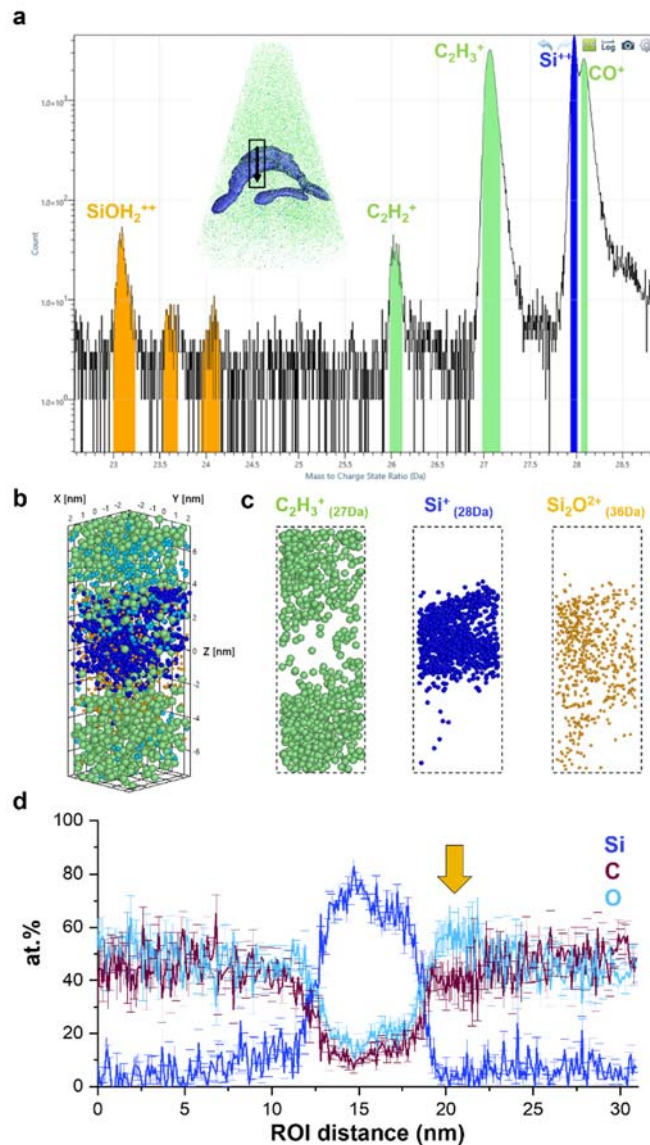


Fig. S5. APT analysis of 1-cycled electrolyte sample. (a) Mass spectrum of cycled electrolyte APT dataset. Note that there is a strong peak split at 28 Da originated to overlapped peaks of CO^+ and Si^+ ions, which is commonly seen in the CO measurement². Inset shows that corresponding 3D atom map. (b) Extracted region of interest ($5 \times 5 \times 15 \text{ nm}^3$) from Fig. 2d. (c) ions distributions: C_2H_3^+ (green), Si^+ (blue), and Si_2O^+ (orange). (d) 1D compositional profiles along the Si nano-fragment in the measurement direction. Note that O enrichment at the interface can be observed (orange arrow).

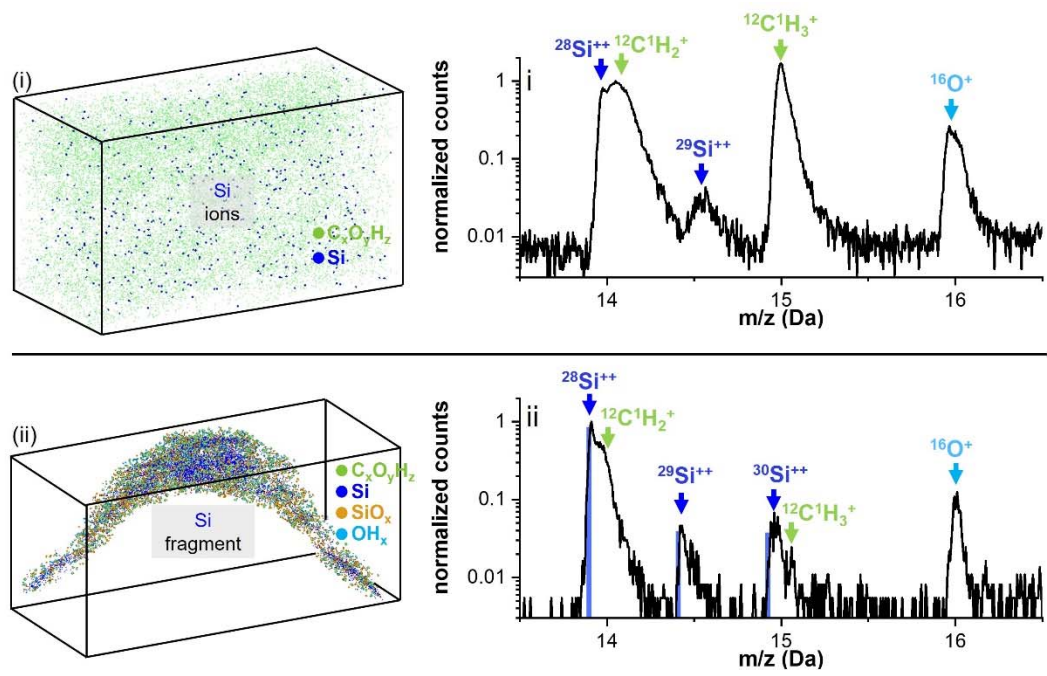


Fig. S6. Mass spectrum of each extracted volume from 1-cycled electrolyte APT dataset (Fig. 2d). Blue lines on the mass spectrum indicate a ratio of natural abundance isotopes of silicon.

APT specimen and TEM lamella preparation from the 10-cycled Si anode

After the cycling for 10 times, the Si anode was collected and rinsed with 1-methyl-2-pyrrolidone (NMP) (anhydrous 95%, Sigma Aldrich) solvent inside the N₂ glovebox. After removing surface residuals, it was dried in a vacuum chamber attached to the glovebox for 1 hr. Subsequently, the sample was loaded to the precision etching coating system (PECS) II (Model 685, Gatan). A 50 nm layer of Cr was deposited on the sample for surface protection. The coated sample was loaded to the dual-beam FIB (FEI Helios Nanolab 600) chamber. APT specimens from the 10-cycled sample were prepared using Ga-ion milling according to ref.³. Three distinguishable interest regions (topmost surface, near-surface, and bulk) were fabricated into the APT specimens. For TEM lamella, first, the surface was coated additionally with e- and Ga-ion beam-induced Pt/C layer. Then the lamella was obtained mostly following the protocol described in ref.⁴.

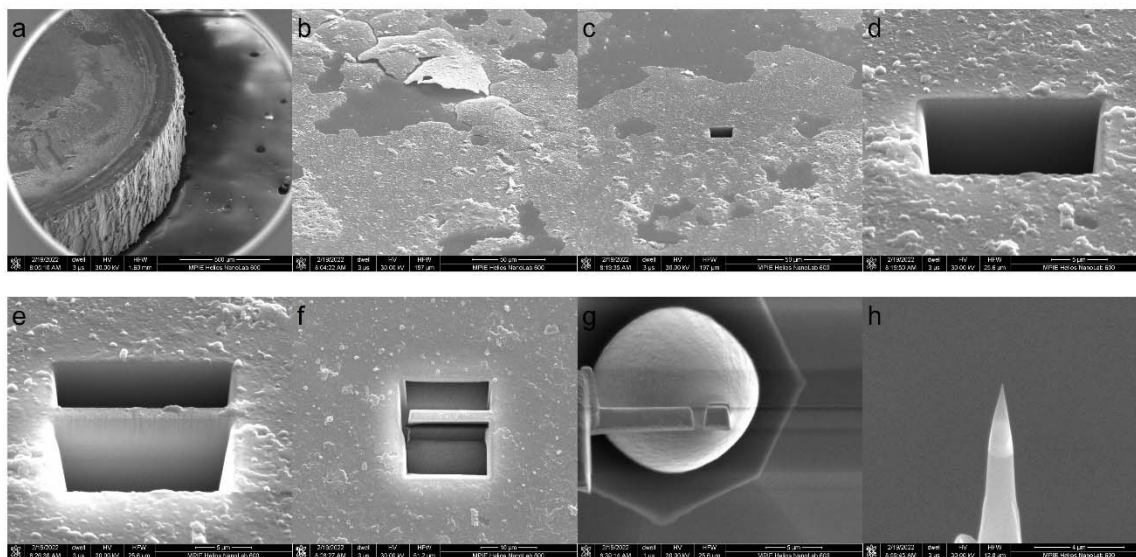


Fig. S7. APT specimen preparation of the 10-cycle Si anode. The disassembled electrode was coated with PECs-Cr layer (~50 nm). (a) 52°-tilted Si anode. (b) FIB/SEM surface image shows that there are delaminated layers of residuals (*i.e.* salt (please see APT/TEM results in S9 and 11)). (c)-(e) Front and back-side cuts. (f) L-shape cut to free the lamella. (g) Mounted APT sample on a commercial Si micro-post. (h) A final APT specimen.

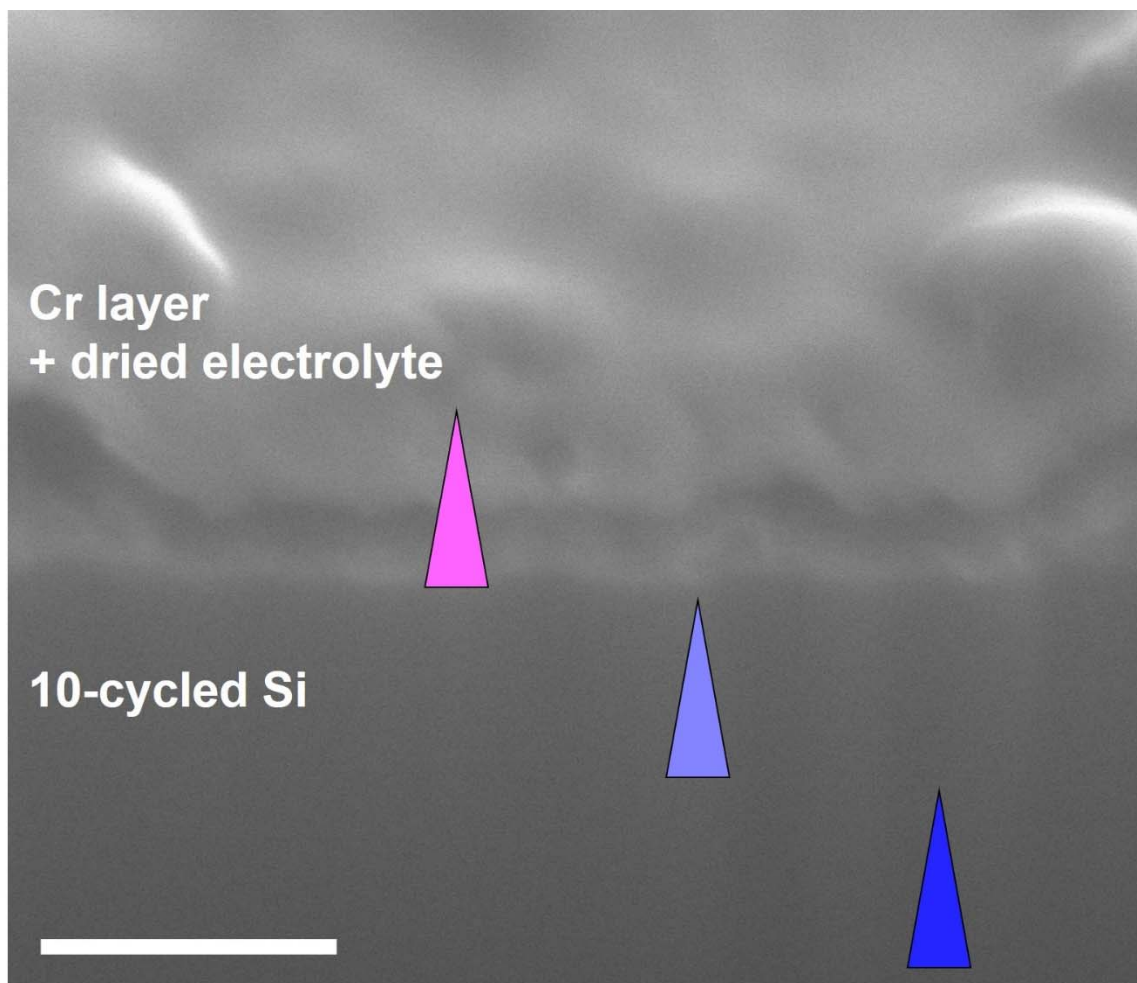


Fig. S8. A cross-sectional FIB/SEM image of the 10-cycled Si anode (scale bar = 500 nm). The colored triangles indicate the regions of three representative APT measurements that are presented in Fig. S9.

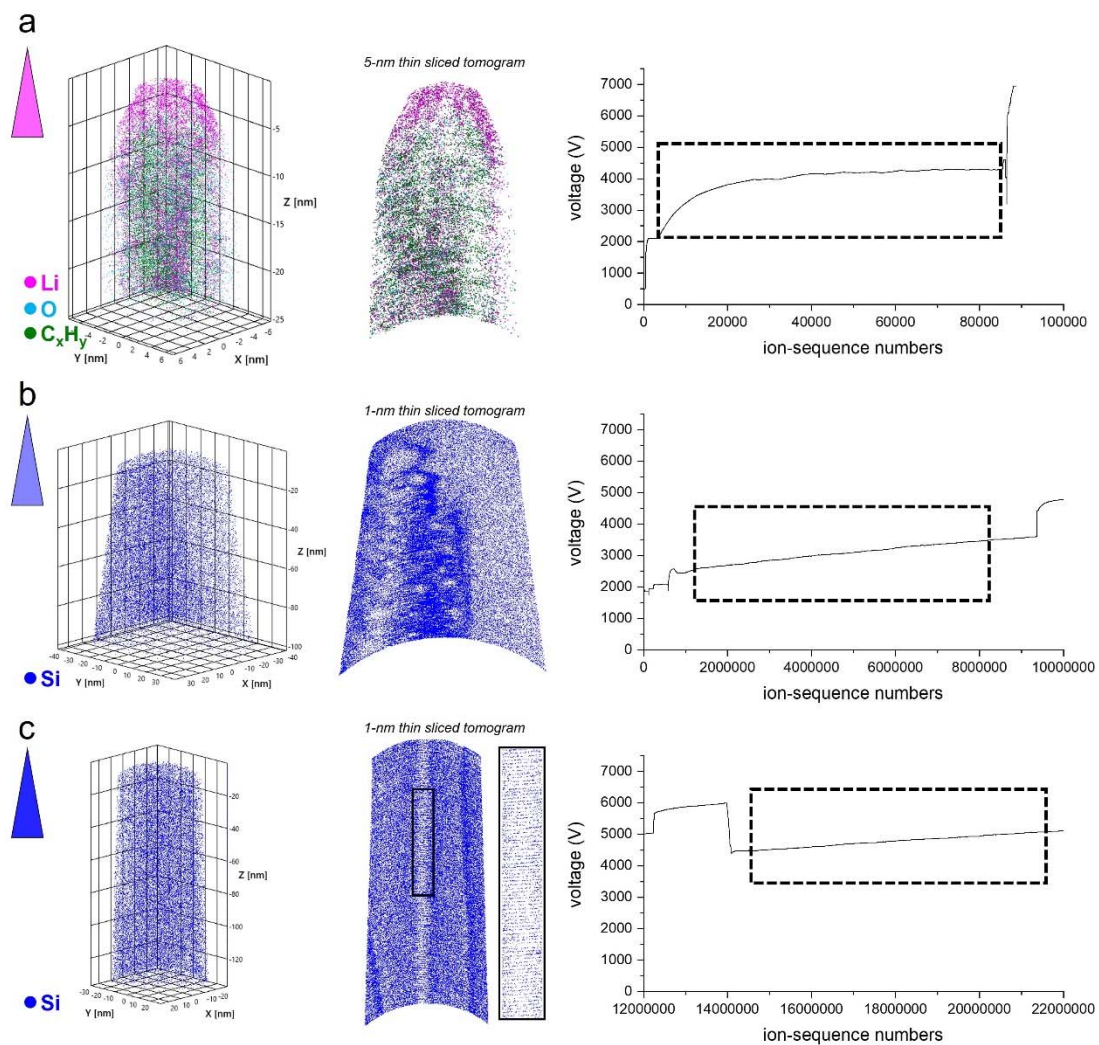


Fig. S9. APT analysis (3D atom map, tomogram, and V-curves) of (a) salt layer, (b) near-surface Si, (c) bottom Si from the 10-cycled Si sample. Note that ambiguous peaks in the APT dataset from the salt layer were not ranged, for instance F (LiC) vs. H₃O or Li₂C vs. C₂H₂ etc.

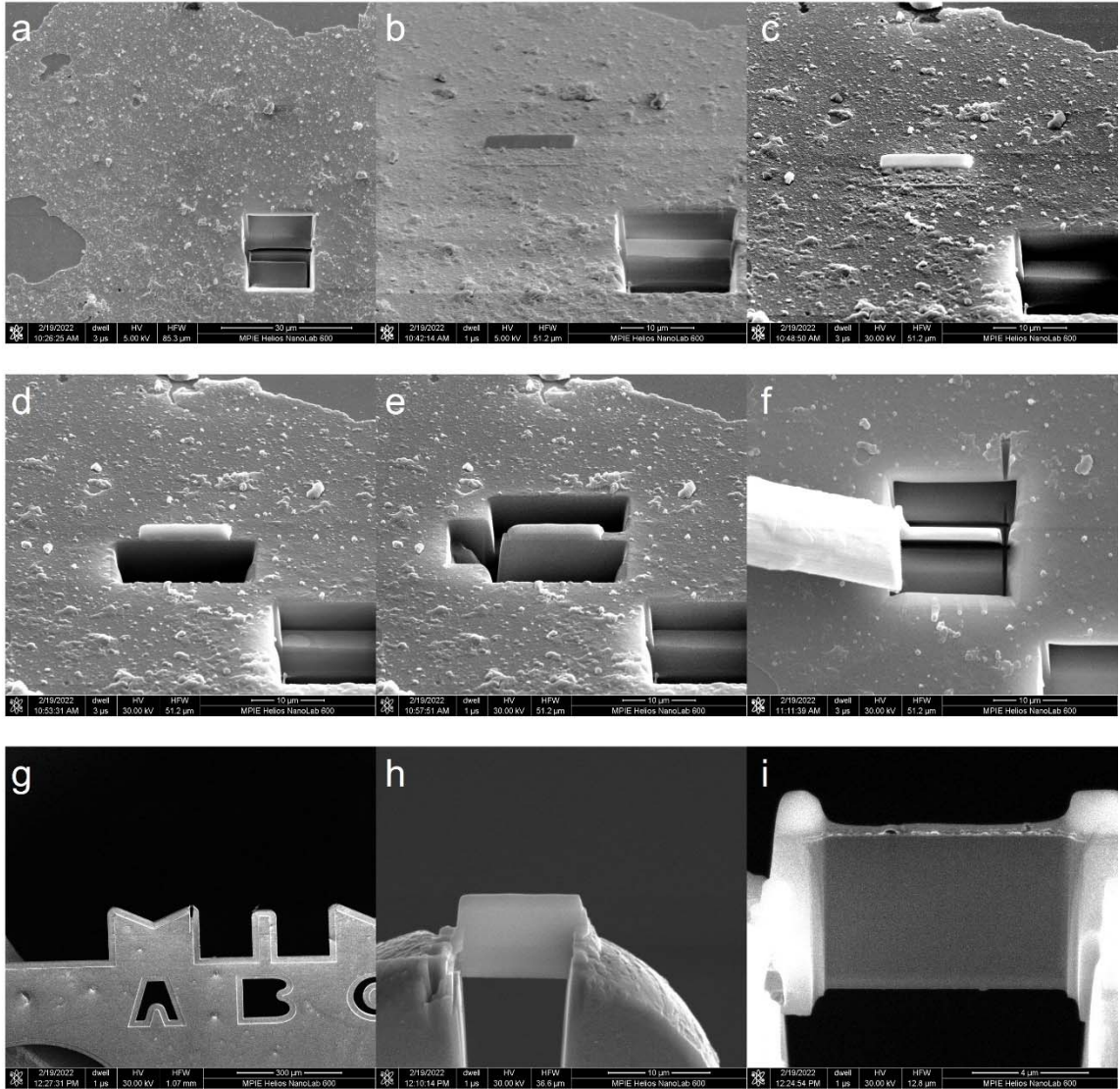


Fig. S10. TEM lamella preparation of the 10-cycled Si sample. (a) FIB/SEM surface image near the APT-site-lift-out region. (b) e-beam Pt/C deposition. (c) ion-beam Pt/C deposition. (d) & (e) Front-side and back-side cuts followed by the L-cut. (f) Attachment to a micro-manipulator. (g) FIB/SEM image of a commercial TEM Cu grid. (h) Mounted TEM lamella on the grid. (i) A final TEM lamella after the thinning process.

TEM measurement

TEM characterization of the cycled Si anode was performed in a JEM-2200FS TEM (JEOL) instrument operating at 200 kV. TEM images were acquired using a TemCam-XF416 pixelated scintillator-based complementary metal-oxide-semiconductor (CMOS) detector from Tietz Video and Image Processing Systems (TVIPS). We used Gatan Microscopy Suite[®] 3 Software to process TEM images, e.g. Fast-Fourier Transformation (FFT) of high-resolution TEM (HRTEM) images. The lamella specimen of the 10-cycled Si anode was tilted close to Si [110] zone for the high resolution imaging of lattice fringes. Fig. S11a shows the interfacial regions between the Pt/C protection, the PECS-Cr, the electrolyte residuals, and the 10-cycled Si anode. Regions of interest have been highlighted in Fig. S11b to show local structure of the electrolyte residuals and the interface between the electrolyte residuals and the Si anodes. Fig. S12&13 present a variety of different defect structures observed in the 10-cycled Si anode.

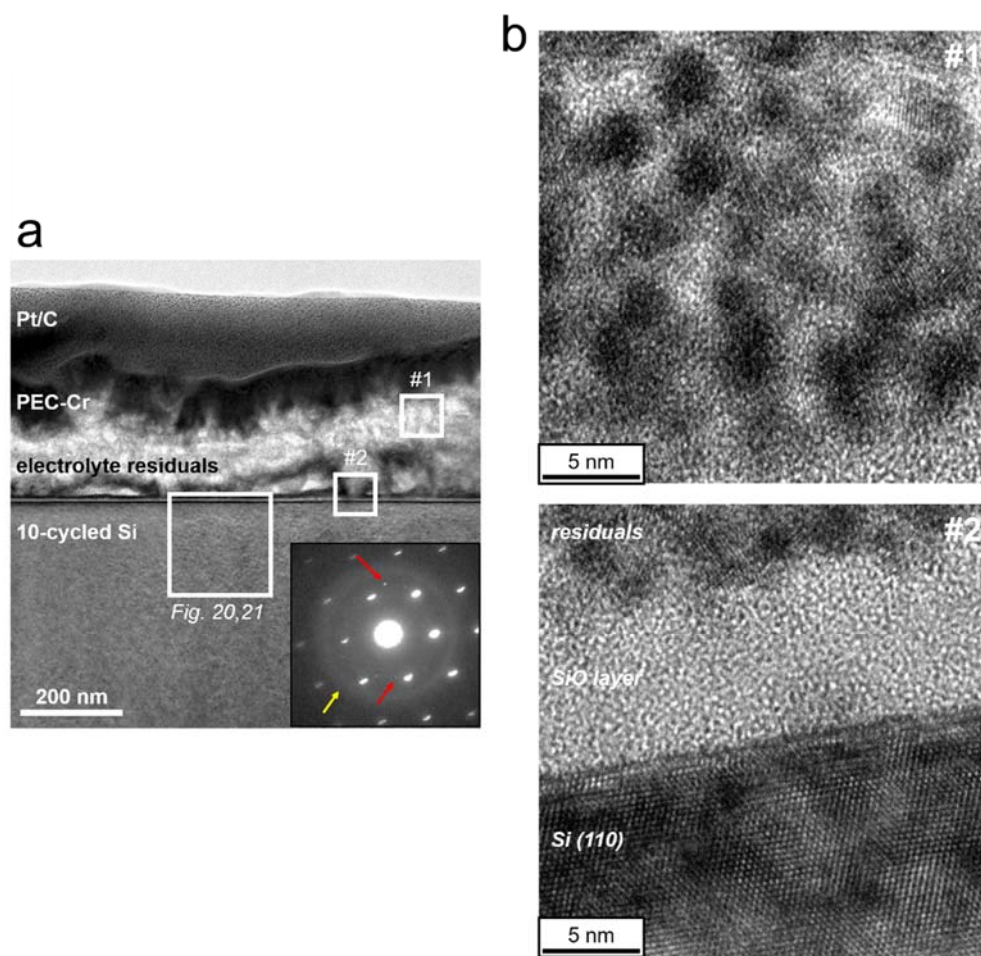


Fig. S11. TEM analysis of the 10-cycle Si. (a) Bright-field (BF) from the top-surface region and (b) high-resolution TEM (HRTEM) images of two small regions as marked with squares in (a). Inset image in **a** shows the complex diffraction patterns with amorphous ring (yellow) and unidentified diffraction points (red). The fast-Fourier transformation (FFT) patterns are measured along [110] Si zone axis.

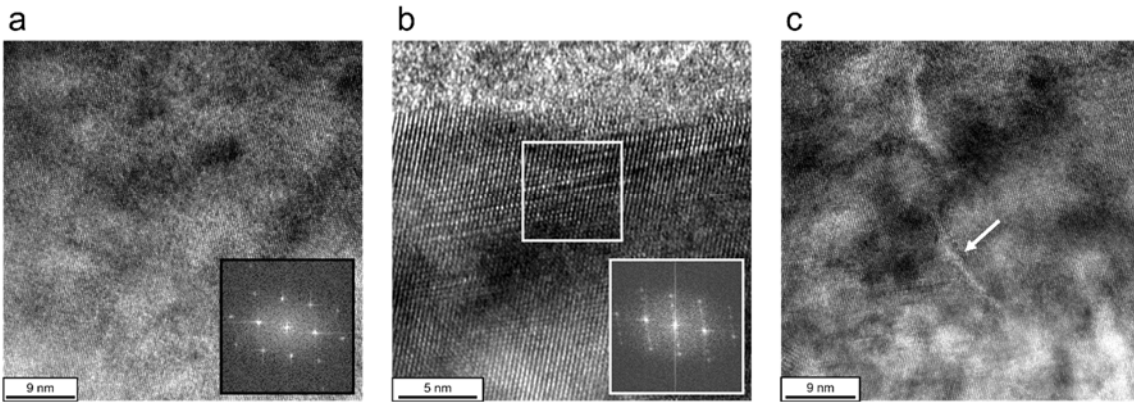


Fig. S12. HRTEM analysis of the 10-cycle Si. (a) Si region with a clear a single-phase Si[110] FFT pattern. (b) Defect sites at near-surface. (c) Defect sites within the Si anode.

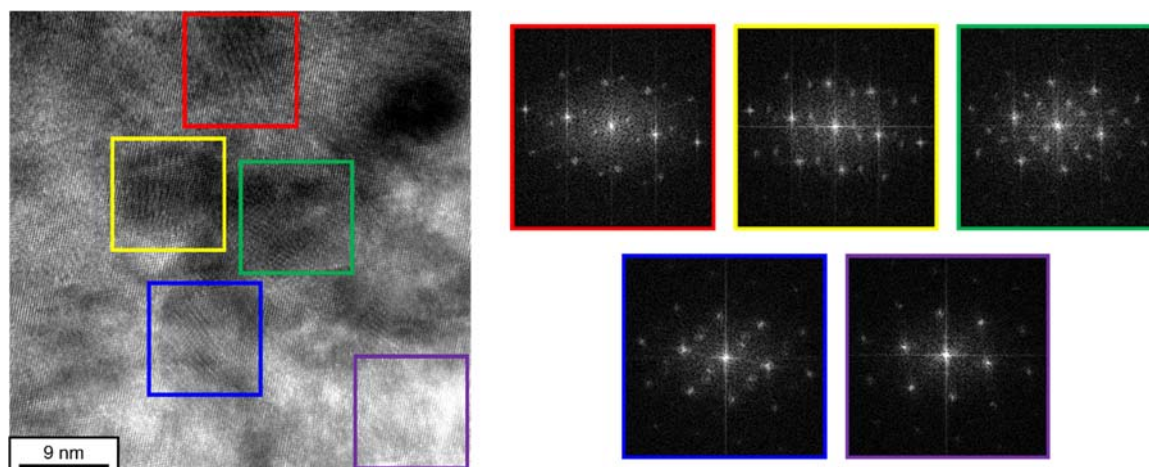


Fig. S13. HRTEM analysis of the 10-cycle Si. Note that these FFT patterns show different types of defects.

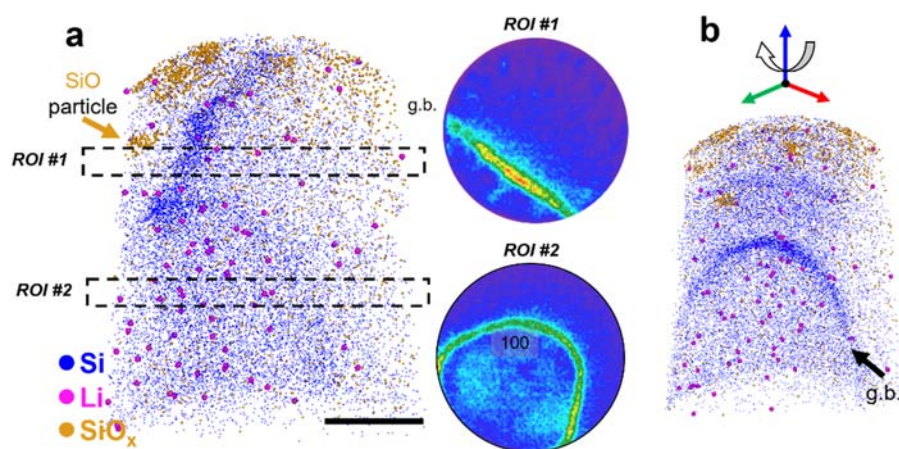


Fig. S14. (a) 3D atom map of the 25-cycle Si anode with Si ion density map. (b) 90°-rotated 3D atom map of 25-cycle Si anode (from Fig. 2f); a scale bar is 20 nm.

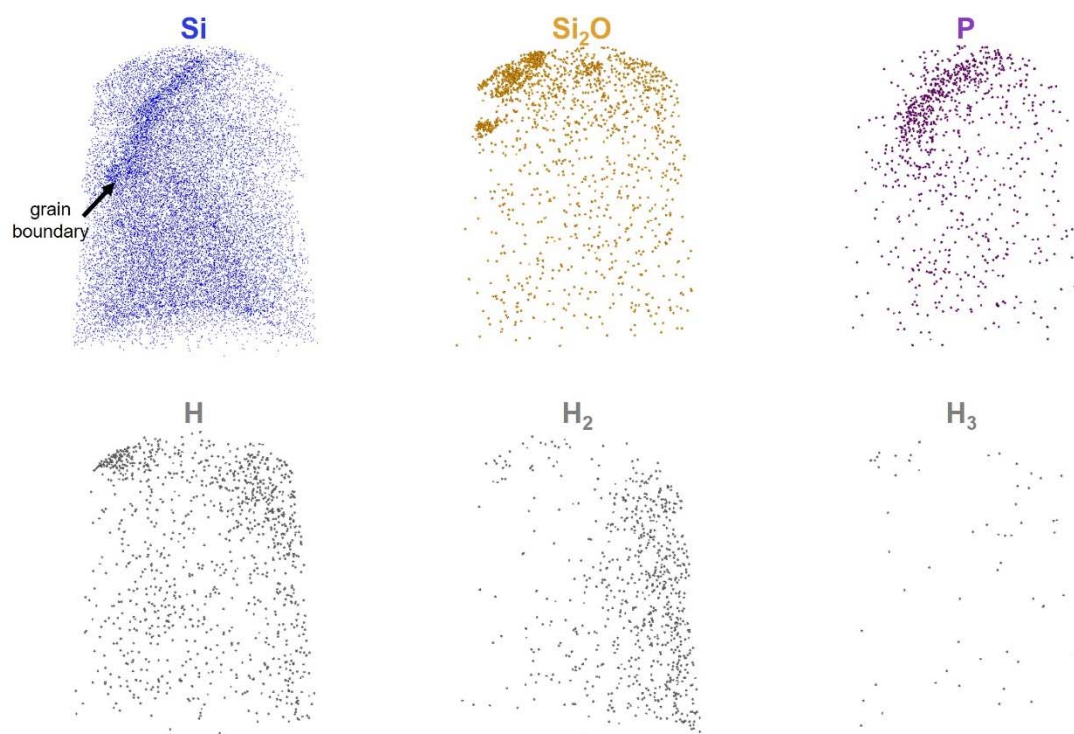


Fig. S15. 3D atomic distributions of Si, Si₂O, P, H, H₂, and H₃ species of the 25-cycled Si. It clearly shows that the peak at 31 Da is not related to H-Si peaks but different species (*i.e.* P). Note that O does not appear at region where P atoms locate.

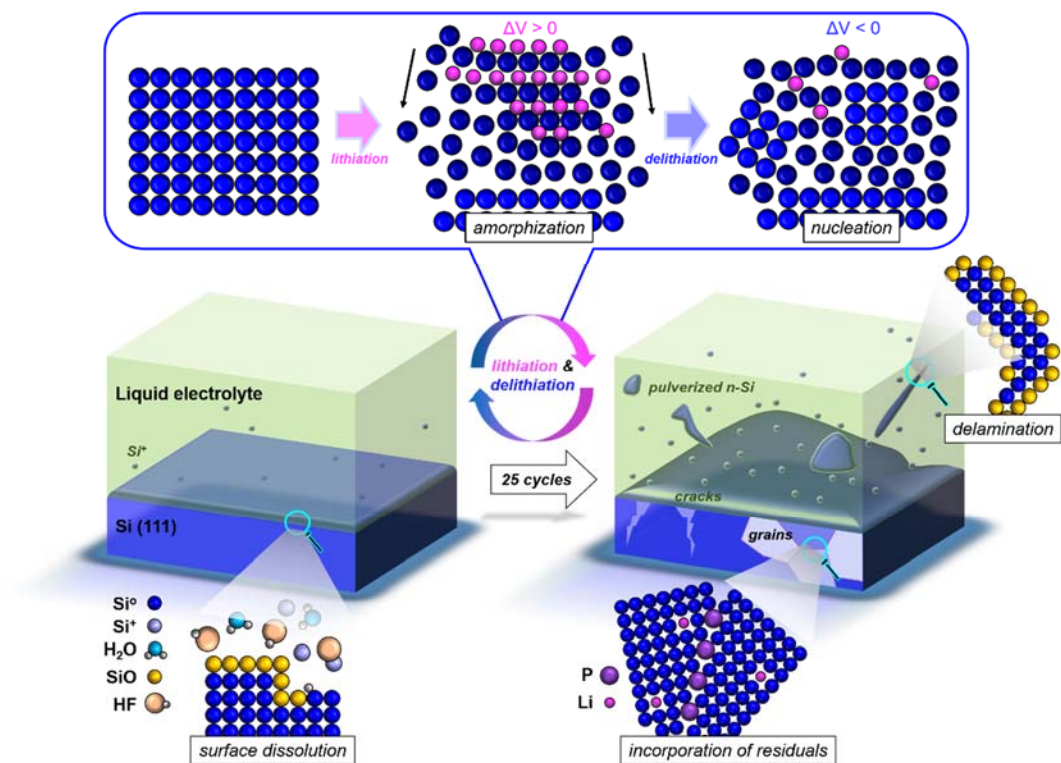


Fig. S16. Schematic illustration of Si anode failure: dissolution, delamination, implementation of electrolyte salt elements, and mechanical-stress relaxation.

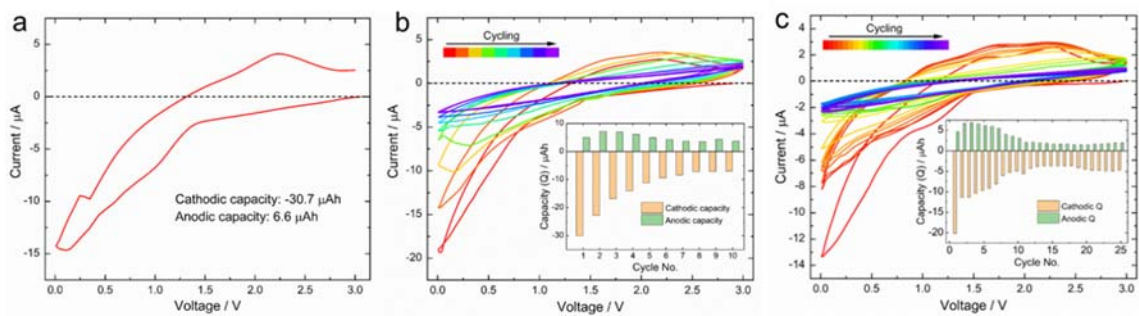


Fig. S17. The voltage profiles of the Li/Si cells after (a) 1, (b) 10, and (c) 25 cycles. Li/Si cells show similar electrochemical behavior during the CV scanning. From the insert figure in panel (b) and (c), evident cathodic capacity fading could be observed during the consecutive 10 and 25 cycles, respectively.

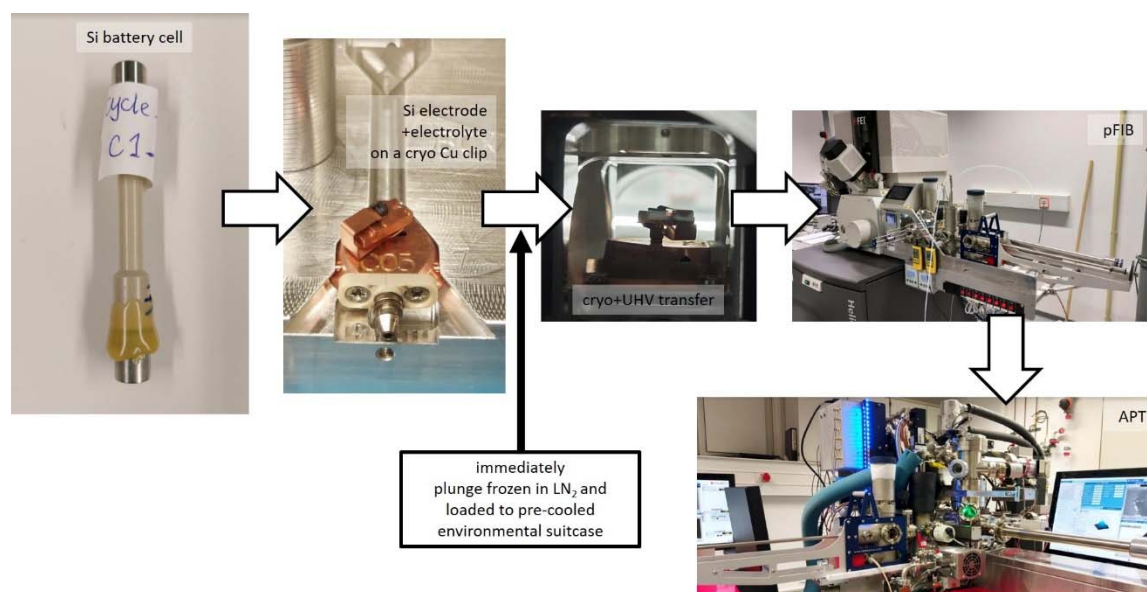


Fig. S18. The protocol of cryo-APT experiment. A battery cell was disassembled inside a N₂ glovebox and the interested cell was mounted on the Cu clip and immediately quenched into LN₂. Subsequently, the clip was loaded to the pre-cooled UHV carry suitcase (-190 °C and 10⁻⁹ mbar) and transferred to Gatan cryo-stage installed plasma-FIB. After final milling, the cold specimen was transferred back to the suitcase maintaining cryo-UHV conditions and was detached from the PFIB and mounted onto a LEAP 5000 XS atom probe system. Finally, the puck was transferred under cryo-UHV conditions to the atom probe analysis chamber. Details on the specific home-made installation are described in Ref.⁵.

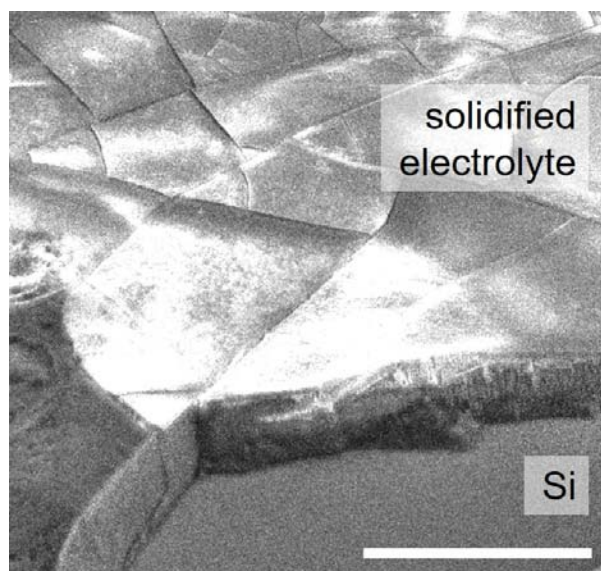


Fig. S19. Xe-plasma FIB/SEM image of frozen liquid electrolyte on the 1-cycle Si electrode. A white scale bar is 100 μm .

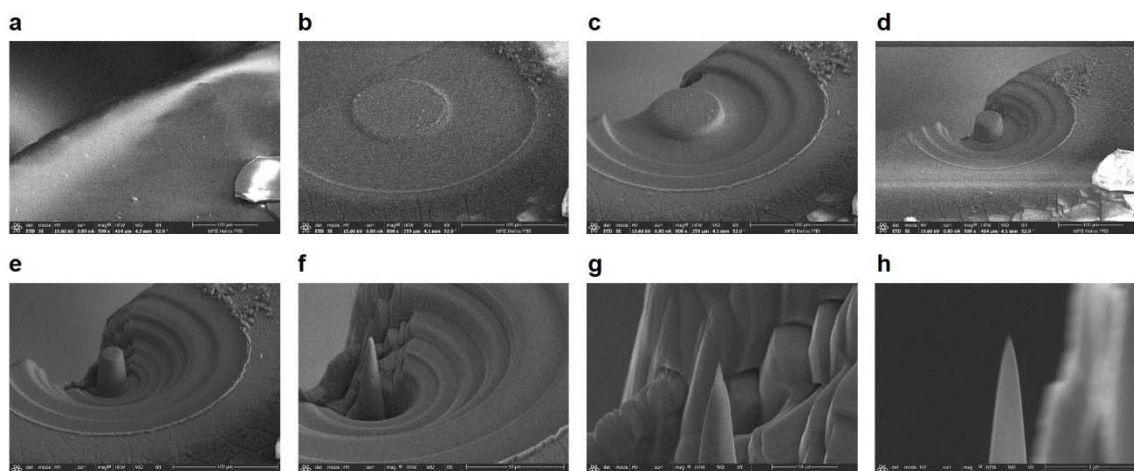


Fig. S20. APT specimen preparation of frozen liquid electrolyte/cryo-Si sample. The Halpin protocol was adapted to obtain a pillar shape⁶. (a) First, an ion-beam-circle pattern of outer diameter of 200 μm and inner diameter of 100 μm was set at 30 kV and 1.3 μA for 10 min. (b)-(e) Then patterns of outer and inner diameters were gradually reduced until inner diameters reach 30 μm with a depth of 50 μm . (f) The ion-beam current was set at 60 nA and the pillar was milled with a circle pattern (outer/inner = 50/10 μm) further down to fabricate into a toberone shape. (g) Once a typical APT specimen geometry was obtained, the ion-beam current was reduced to 1 nA. (f) The final milling process was done at ion-beam current of 0.3 nA.

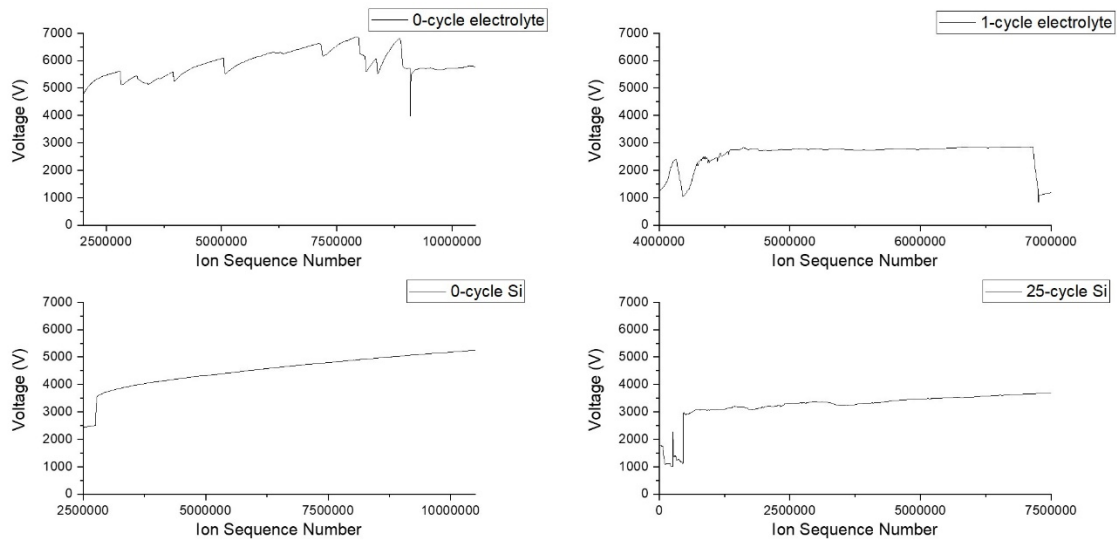


Fig. S21. Voltage curve of each cryo-measurement: 0-cycle electrolyte, 0-cycle Si anode, 1-cycle electrolyte, 1-cycle electrolyte containing n-Si debris, 25-cycle Si anode.

References

1. Hille, E. & Märk, T. D. Cross section for single and double ionization of carbon monoxide by electron impact from threshold up to 180 eV. *J. Chem. Phys.* **69**, 4600–4605 (1978).
2. London, A. J. Quantifying Uncertainty from Mass-Peak Overlaps in Atom Probe Microscopy. *Microsc. Microanal.* **25**, 378–388 (2019).
3. Thompson, K. *et al.* In situ site-specific specimen preparation for atom probe tomography. *Ultramicroscopy* **107**, 131–139 (2007).
4. Giannuzzi, L. A. & Stevie, F. A. A review of focused ion beam milling techniques for TEM specimen preparation. *Micron* **30**, 197–204 (1999).
5. Stephenson, L. T. *et al.* The Laplace project: an integrated suite for correlative atom probe tomography and electron microscopy under cryogenic and UHV conditions. *PLoS One* **13**, e0209211 (2018).
6. Halpin, J. E. *et al.* An in-situ approach for preparing atom probe tomography specimens by xenon plasma-focussed ion beam. *Ultramicroscopy* **202**, 121–127 (2019).